

AperTO - Archivio Istituzionale Open Access dell'Università di Torino

## Modulational Instability, Wave Breaking, and Formation of Large-Scale Dipoles in the Atmosphere

### This is the author's manuscript

*Original Citation:*

*Availability:*

This version is available <http://hdl.handle.net/2318/139422> since

*Published version:*

DOI:10.1103/PhysRevLett.110.184504

*Terms of use:*

Open Access

Anyone can freely access the full text of works made available as "Open Access". Works made available under a Creative Commons license can be used according to the terms and conditions of said license. Use of all other works requires consent of the right holder (author or publisher) if not exempted from copyright protection by the applicable law.

(Article begins on next page)



## Modulational Instability, Wave Breaking, and Formation of Large-Scale Dipoles in the Atmosphere

A. Iafrati,<sup>1</sup> A. Babanin,<sup>2</sup> and M. Onorato<sup>3,4</sup>

<sup>1</sup>*CNR-INSEAN, Italian Ship Model Basin, Roma 00128, Italy*

<sup>2</sup>*Swinburne University of Technology, Hawthorn, Victoria 3122, Australia*

<sup>3</sup>*Dipartimento di Fisica, Università di Torino, Via P. Giuria 1, Torino 10125, Italy*

<sup>4</sup>*INFN, Sezione di Torino, Via P. Giuria 1, Torino 10125, Italy*

(Received 27 August 2012; published 3 May 2013)

We use direct numerical simulation of the Navier-Stokes equations for a two-phase flow (water and air) to study the dynamics of the modulational instability of free surface waves and its contribution to the interaction between the ocean and atmosphere. If the steepness of the initial wave exceeds a threshold value, we observe wave-breaking events and the formation of large-scale dipole structures in the air. Because of the multiple steepening and breaking of the waves under unstable wave packets, a train of dipoles is released in the atmosphere; those dipoles propagate at a height comparable with the wavelength. The amount of energy dissipated by the breaker in water and air is considered, and contrary to expectations, we observe that the energy dissipation in air is greater than that in water. The possible consequences on the wave modeling and on the exchange of aerosols and gases between air and water are discussed.

DOI: [10.1103/PhysRevLett.110.184504](https://doi.org/10.1103/PhysRevLett.110.184504)

PACS numbers: 47.35.-i, 47.20.-k, 92.10.-c

The modulational instability, also known as the Benjamin Feir instability, is a well-known universal phenomenon that takes place in many different fields of physics such as surface gravity waves, plasma physics, and nonlinear optics (see the recent historical review in Ref. [1]). The basic idea is that a sufficiently steep sinusoidal wave train may become unstable if perturbed by a long enough perturbation; as a result of the modulation, a single wave in the group may reach an amplitude that is at most 3 times the initial one [2,3]. It is a threshold mechanism; therefore, for example, for surface gravity waves at an infinite water depth, a wave is unstable if  $2\sqrt{2}k_0A_0 > \Delta k/k_0$ , where  $k_0$  is the wave number of the sinusoidal wave (carrier wave),  $\Delta k$  is the wave number of the perturbation, and  $A_0$  is the amplitude of the initial wave. The modulational instability, discovered in the 1960s, has recently received attention because it has been recognized as a possible mechanism of formation of rogue waves [4,5]. The standard mathematical tool used to describe such physical phenomena is the nonlinear Schrödinger equation (NLS), i.e., a weakly nonlinear, narrow band approximation of some primitive equations of motion. The beauty of such an equation is that it is integrable, and many analytical solutions can be written explicitly. For example, breather solutions [3] have been considered as prototypes of rogue waves [6,7]; they have been observed experimentally both in surface gravity waves and in nonlinear optics [2,8–10].

Concerning ocean waves, besides the NLS approach, computations of nonviscous, fully nonlinear, potential equations have been performed [11,12]. However, such an approach only predicts the breaking occurrence but does not furnish any prediction beyond the breaking onset.

Moreover, so far none of the aforementioned literature has ever considered the effects of the modulation instability on the fluid above the free surface. As far as we know, this is the first attempt to investigate the dynamics of air on water during the modulation process. This is made possible by simulating the Navier-Stokes equation for a two-phase flow. This approach allows us to investigate conditions that are beyond the formal applicability of the NLS equation: for example, it is well-known that if the initial wave steepness is great enough, the NLS equation is not able to accurately describe the dynamics because wave breaking takes place [13,14]. For steep waves and particularly those close to the breaking onset, vorticity is generated by viscous effects at the interface and by the topological change of the interface in the case of the bubble entrainment processes. The breaking of surface waves, as an oceanic phenomenon [15], is important across a very broad range of applications related to wave dynamics and studies of atmospheric boundary layer, air-sea interactions, and upper ocean turbulence mixing, with respective connections to the large-scale processes including ocean circulation, weather, and climate [16]. Modulational instability has become also relevant in engineering applications [17] for studying the interaction of waves and structures.

In the present work, the two fluids are approximated as a single one with density and viscosity smoothly varying across the interface. The continuity and momentum equations (Navier-Stokes) are discretized over a nonstaggered grid layout with a second-order finite difference scheme. Cartesian velocities, pressure, and physical properties are defined at the center of the cells, whereas volume fluxes are defined at the midpoint of the cell faces. A fractional step

approach is used: the pressure contribution is neglected when integrating the momentum equation (predictor step), and it is reintroduced when the continuity equation is enforced (corrector step) (see Refs. [18,19] for a more detailed discussion on the numerical method). The jump in the fluid properties is spread across a small neighborhood of the interface. A similar spreading is used for the surface tension forces for which a continuum model is adopted [20]. The air-water interface is captured as the zero-level of a distance function from the interface  $d(\mathbf{x}, t)$  that, at  $t = 0$ , is initialized as  $d > 0$  in water and  $d < 0$  in air. Fluid properties are related to the distance  $d$  by the equation

$$f(d) = f_a + (f_w - f_a)H_\delta(d), \quad (1)$$

where  $H_\delta(d)$  is a smooth step function and  $\delta$  is the half-thickness of the transition region. The distance function is advected by the velocity field  $\mathbf{u}$  by the equation

$$\frac{\partial d}{\partial t} + \mathbf{u} \cdot \nabla d = 0, \quad (2)$$

and the interface is located as the  $d = 0$  level. The above equation is discretized with the same scheme adopted for the convective terms in the Navier-Stokes equation, and it is integrated in time using a third-order Runge-Kutta scheme. At the end of the step, the free surface is located as the  $d = 0$  level and the distance is reinitialized. The numerical model has been carefully validated in previous works [19,21]. The analysis showed that accurate solutions can be obtained, provided the transition region covers a sufficiently large number of grid points. Five grid points are generally enough, [19], but the minimum number depends to some extent on the Reynolds number.

In our simulations, we consider the standard modulational instability process as, for example, the one produced experimentally in Ref. [22]. The initial surface elevation is characterized by a perturbed sinusoidal free surface elevation

$$\eta(x, t = 0) = A_0 \cos(k_0 x) + A_1 [\cos(k^+ x) + \cos(k^- x)], \quad (3)$$

where  $\eta(x, t)$  denotes the free surface elevation at location  $x$  and time  $t$ ,  $k_0$  is the wave number of the carrier wave, and  $k^\pm = k_0 \pm \Delta k$  with  $\Delta k$  the wave number of the perturbation. In Eq. (3),  $A_0$  and  $A_1$  indicate the amplitude of the fundamental and perturbation components, respectively. The simulations presented hereafter are characterized by a steepness  $\epsilon_0 = k_0 A_0$  that is varied from 0.1 to 0.18, with a step 0.02. The sideband components are placed at  $\Delta k = k_0/5$ , and their amplitude is  $A_1 = 0.1A_0$ . The conditions are essentially similar to those used in Refs. [12,23] and correspond to the early stages of an Akhmediev breather [3].

Because the typical time scale of the modulational instability is on the order of 100 periods, to reduce the computational effort, the initial development of the instability is described by a fully nonlinear, potential flow model. Hence, some instant before the onset of the breaking, the potential flow solution is used as an initial condition for

the Navier-Stokes simulations [24]. We underline that, different from the present work, in Refs. [18,25] the initial conditions that lead to breaking were characterized by a steep ( $\epsilon_0 > 0.33$ ) third-order Stokes wave (without any perturbation) that broke after a few wavelengths, and no modulational instability process was investigated.

In the following, for convenience, results are presented in dimensional form. Simulations are carried out for a carrier wave of wavelength  $\lambda_0 = 0.60$  m, with  $g = 9.81$  ms<sup>-2</sup>. The computational domain spans from  $x = -1.5$  m to  $x = 1.5$  m horizontally and from  $y = -2$  m up to  $y = 0.6$  m above the still water level vertically. It is discretized with a uniform grid spacing in the horizontal direction with  $\Delta x = 1/1024$  m. Vertically, from  $y = -0.15$  m to 0.15 m, the grid spacing is uniform and equal to  $\Delta x$ , whereas it grows geometrically by a factor of  $\alpha = 1.03$  towards the upper and lower boundaries. This gives a total of  $3072 \times 672$  grid cells (numerical simulations have been performed also on a coarse grid of  $1536 \times 336$  in order to see the effects of the resolution). The total thickness of the transition region is 0.01 m, so that the density jump is spread across about 10 grid cells. The surface tension is included in the Navier-Stokes simulation and taken as  $\sigma = 0.073$  N m<sup>-1</sup>; the following values of densities and viscosity of air and water are considered:  $\rho_w = 1000$  kg m<sup>-3</sup>,  $\rho_a = 1.25$  kg m<sup>-3</sup>,  $\mu_w = 10^{-3}$  kg m<sup>-1</sup> s<sup>-1</sup>, and  $\mu_a = 1.8 \times 10^{-5}$  kg m<sup>-1</sup> s<sup>-1</sup>.

The process observed in the simulation corresponds to the standard modulational instability (exponential growth of the sidebands) up to the point where the wave group reaches its strongly nonlinear regime. For  $\epsilon_0 = 0.10$ , the perturbation reaches a maximum and then returns back to the original conditions. This is not the case for  $\epsilon_0 \geq 0.12$ , for which wave breaking is observed (see also Ref. [12]). In Fig. 1, a breaking event is shown for  $\epsilon_0 = 0.18$ . The sequence shows the formation of the jet, which plunges onto the water and entraps air. The jet then bounces on the free surface and plunges again onto the free surface, thus leading to the entrainment of a second air bubble. A few droplets of water in air are also visible; a small amount of vorticity is also released beneath the surface.

Of particular interest is the dynamics of the air flow. In Fig. 2, we show a sequence of snapshots of the water and air domain where the formation and detachment of a dipole structure is highlighted for  $\epsilon_0 = 0.16$ . The fast steepening of the wave profile and the subsequent breaking causes the air flow to separate from the crest, giving rise to a large positive-vorticity structure. This vortex structure interacts with the free surface leading to the formation of vorticity of opposite sign; eventually a dipole is generated and propagates upwards under the self-induced velocity. It is worth noting that the occurrence of flow separation and strong vorticity production are strongly enhanced by the breaking occurrence, whereas such phenomena are not found in the nonbreaking case with  $\epsilon_0 = 0.10$ .

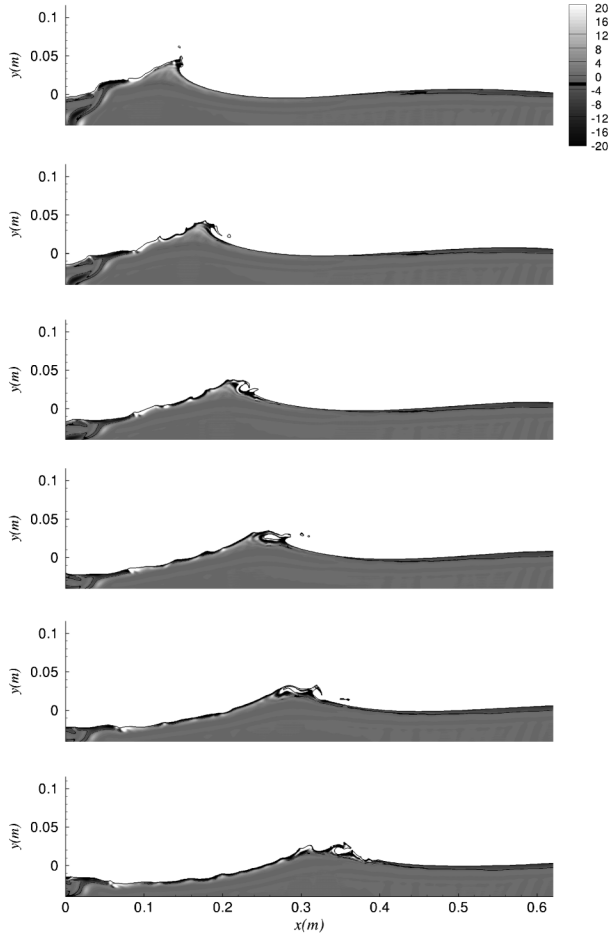


FIG. 1. Breaking event for  $\epsilon_0 = 0.18$ . Vorticity, in  $s^{-1}$ , is represented in gray scale.

Because the group velocity is half the phase velocity, each single wave that passes below the group (at its maximum height) breaks. The result is that a series of breaking events take place and dipoles are released into the atmosphere as shown in Fig. 3. Two things should be noted: (i) the height of the highest dipoles is on the order of the wavelength, and (ii) a large amount of vorticity is observed in the air and not in the water. One major question to be answered, especially in the spirit of modeling the dissipation term in the wave forecasting models [26,27], is the amount of energy dissipated during a wave breaking or a sequence of breaking events. Therefore, a quantitative estimate of the dissipated energy both in air and water can be obtained by integrating the viscous stresses over the air and water domains,

$$\epsilon_{\text{diss}}^w(t) = \mu_w \int_{d \geq \delta} 2e_{ij} \frac{\partial u_i}{\partial x_j} dx dy, \quad (4)$$

$$\epsilon_{\text{diss}}^a(t) = \mu_a \int_{d < -\delta} 2e_{ij} \frac{\partial u_i}{\partial x_j} dx dy, \quad (5)$$

where  $e_{ij}$  is the symmetric part of the strain tensor. In Figs. 4 and 5, we show the dissipation functions in air and water

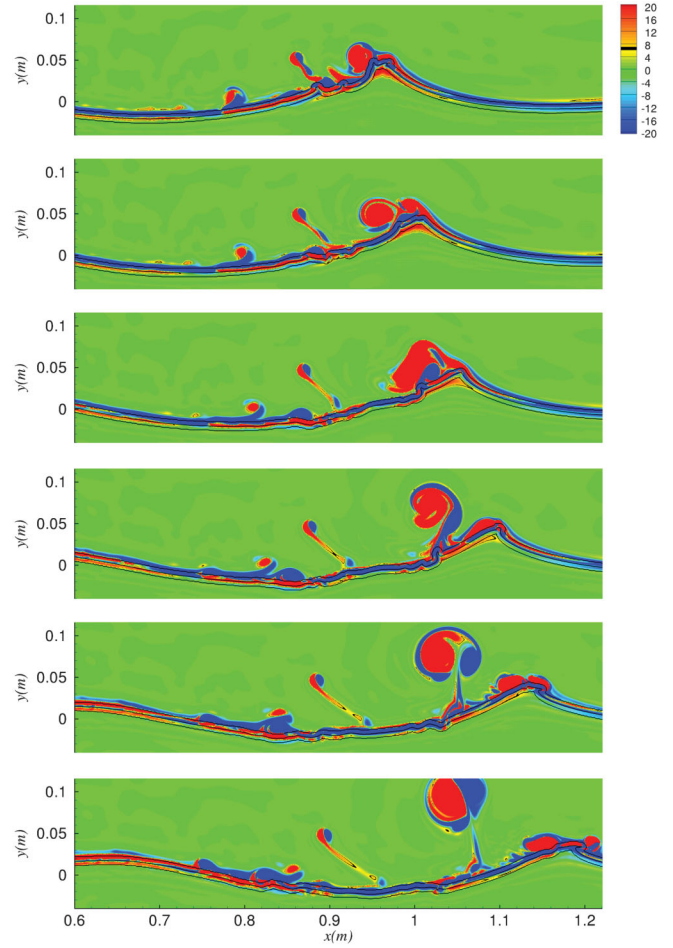


FIG. 2 (color). Formation of a dipole in air as a consequence of the wave breaking. Results refer to  $\epsilon_0 = 0.16$ . Vorticity, in  $s^{-1}$ , is represented in color scale.

normalized by the initial energy of the water and wave period,  $T$ , as a function of time, nondimensionalized by  $T$ , for simulations with steepness  $\epsilon_0 = 0.12$  and  $\epsilon_0 = 0.16$ , respectively; the origin of the time axis is set to the time at which the Navier-Stokes simulations take over potential code simulation. Both curves display a recurrent growth of the dissipation levels concurrent with the breaking events. The results indicate that an energy fraction is first transferred to the air during the steepening and breaking processes and then dissipated by the viscous stresses afterwards. The figures also include the simulations performed on a coarser

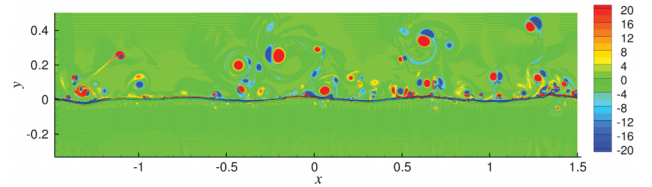


FIG. 3 (color). Vorticity field in a portion of the computational domain for initial steepness  $\epsilon_0 = 0.18$ . The Supplemental Material contains an animation of the simulation [29].

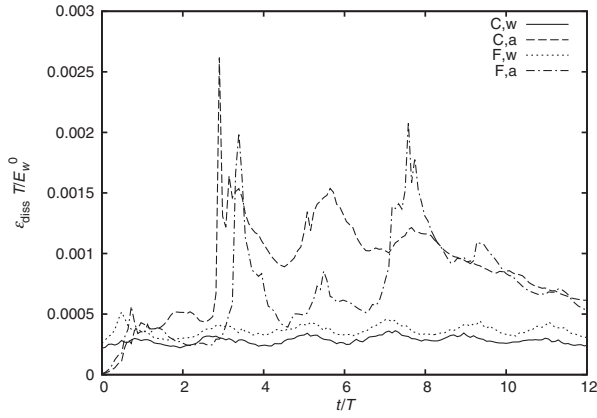


FIG. 4. Dissipation nondimensionalized with period  $T$  and total energy in the water  $E_w^0$  at  $t = 0$  as a function of nondimensional time for water (denoted with “w”) and air (denoted with “a”). The initial steepness is 0.12. Solutions for fine (F) and coarse (C) grids are plotted.

grid. As expected, because of the chaotic behavior of the Navier-Stokes equation, the breaking (which is related to the peaks in the figures), being a threshold mechanism, does not happen exactly in the same place with the same intensity in the two simulations with different resolutions. Nevertheless, from both simulations, one can evince that the dissipation is higher in the air than in the water.

In order to show how relevant the energy dissipation in air is in comparison to the corresponding dissipation in water, we consider the following integrated quantity:

$$E_{\text{diss}}(t) = \int_0^t \varepsilon_{\text{diss}}(t') dt'. \quad (6)$$

The integral is considered for both water and air. The time histories of the integrals of the viscous dissipation terms in the two media are shown in Fig. 6 for the four different steepnesses. It is interesting to observe that in nondimensional form, the solutions for the four different cases almost overlap; at the end of the simulations the total

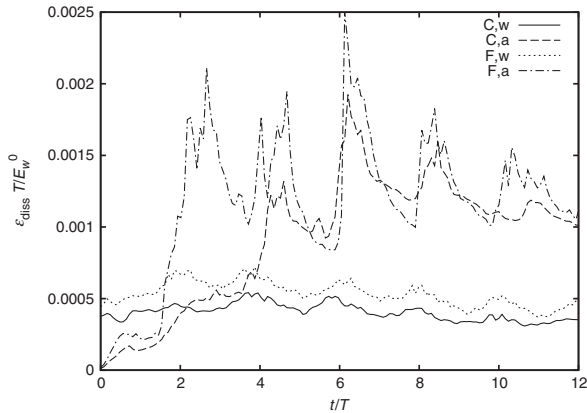


FIG. 5. Same as Fig. 4 but for an initial steepness of 0.16.

energy fraction dissipated in the air is about three times that in water.

*Discussion.*—Modulated waves of different initial steepnesses have been analyzed using the two-phase flow NS equation. For initial steepness greater or equal to 0.12, multiple breaking events have been observed. Spray is the natural consequence of the wave breaking. Droplets of water are thrown in the air; some of these particles are so small (aerosols) that they can remain in the air for a very long time, forming condensation nuclei and affecting incoming solar radiation. Vortices, observed in our simulations, can in principle transport aerosols (not resolved in our simulations) up to the height of the wave lengths (this can be even underestimated because of the presence of the solid boundary at the top of the computational domain). Such phenomena may be relevant for climate modeling.

Even bearing in mind the limitations of the numerical scheme, the results indicate that in the present case (i.e., breaking due to modulational instability) the dissipation of the energy is mostly concentrated in the air side. We stress that it is a common practice to estimate the energy loss due to wave breaking by looking at the amount of energy dissipated in the water; see for example Ref. [28]. Such measurements are the bases for the construction of the dissipation function in operational wave forecasting modeling [27]. We also underline that our simulations correspond to the propagation of waves without the presence of external wind: what would be the consequences of a turbulent wind on the generation of vorticity during breaking event is under investigation.

Another important limitation of the simulations concerns the use of a two-dimensional assumption for the flow, i.e., long crested waves. We expect that three-dimensional effects may take place and alter the dynamics of the breaking process and of the associated vorticity production.

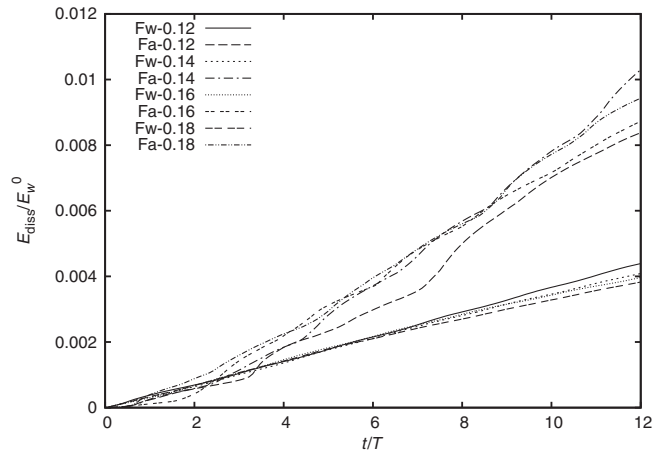


FIG. 6. Integrated dissipation for different values of the steepness in water (w) and air (a).

M.O. was funded by the EU project Extreme Seas (SCP8-GA-2009-234175) and by ONR Grant No. N000141010991. Dr. Proment and Dr. Giulinicco are acknowledged for discussion. The work by A.I. was funded by the Flagship Project RITMARE, The Italian Research for the Sea, coordinated by the Italian National Research Council and funded by the Italian Ministry of Education, University and Research within the National Research Program 2011–2013.

- 
- [1] V. Zakharov and L. Ostrovsky, *Physica (Amsterdam)* **238D**, 540 (2009).
- [2] A. Chabchoub, N.P. Hoffmann, and N. Akhmediev, *Phys. Rev. Lett.* **106**, 204502 (2011).
- [3] N. Akhmediev, V. Eleonskii, and N. Kulagin, *Theor. Math. Phys.* **72**, 809 (1987).
- [4] M. Onorato, A.R. Osborne, M. Serio, and S. Bertone, *Phys. Rev. Lett.* **86**, 5831 (2001).
- [5] P. A. E. M. Janssen, *J. Phys. Oceanogr.* **33**, 863 (2003).
- [6] A. Osborne, M. Onorato, and M. Serio, *Phys. Lett. A* **275**, 386 (2000).
- [7] K. B. Dysthe and K. Trulsen, *Phys. Scr.* **T82**, 48 (1999).
- [8] G. Clauss, M. Klein, and M. Onorato, in *Proceedings of the ASME 2011 30th International Conference on Ocean, Offshore and Arctic Engineering OMAE2011, Rotterdam, The Netherlands, 2011* (American Society of Mechanical Engineers, New York, 2011), Vol. 2, p. 417.
- [9] B. Kibler, J. Fatome, C. Finot, G. Millot, F. Dias, G. Genty, N. Akhmediev, and J. Dudley, *Nat. Phys.* **6**, 790 (2010).
- [10] B. Kibler, J. Fatome, C. Finot, G. Millot, G. Genty, B. Wetzl, N. Akhmediev, F. Dias, and J.M. Dudley, *Sci. Rep.* **2**, 463 (2012).
- [11] A. Dyachenko and V. Zakharov, *JETP Lett.* **88**, 307 (2008).
- [12] A. Babanin, D. Chalikov, I. Young, and I. Savelyev, *Geophys. Res. Lett.* **34**, L07605 (2007).
- [13] K. Henderson, D. Peregrine, and J. Dold, *Wave Motion* **29**, 341 (1999).
- [14] A. Babanin, T. Waseda, T. Kinoshita, and A. Toffoli, *J. Phys. Oceanogr.* **41**, 145 (2011).
- [15] A. Babanin, *Breaking and Dissipation of Ocean Surface Waves* (Cambridge University Press, Cambridge, England, 2011).
- [16] L. Cavaleri, B. Fox-Kemper, and M. Hemer, *Bull. Am. Meteorol. Soc.* **93**, 1651 (2012).
- [17] M. Onorato, D. Proment, G. Clauss, and M. Klein, *PLoS ONE* **8**, e54629 (2013).
- [18] A. Iafrazi, *J. Fluid Mech.* **622**, 371 (2009).
- [19] A. Iafrazi and E. Campana, *J. Fluid Mech.* **529**, 311 (2005).
- [20] J. Brackbill, D. Kothe, and C. Zemach, *J. Comput. Phys.* **100**, 335 (1992).
- [21] A. Iafrazi, A. Di Mascio, and E. F. Campana, *Int. J. Numer. Methods Fluids* **35**, 281 (2001).
- [22] M.P. Tulin and T. Waseda, *J. Fluid Mech.* **378**, 197 (1999).
- [23] J. Song and M. Banner, *J. Phys. Oceanogr.* **32**, 2541 (2002).
- [24] A. Iafrazi, M. Onorato, and A. Babanin, in *29th ONR Symposium on Naval Hydrodynamics, Gothenburg, Sweden, 2012* (Curran Associates Inc., New York, 2013).
- [25] A. Iafrazi, *J. Geophys. Res.* **116**, C07024 (2011).
- [26] G. Komen, L. Cavaleri, M. Donelan, K. Hasselmann, H. Hasselmann, and P. Janssen, *Dynamics and Modeling of Ocean Waves* (Cambridge University Press, Cambridge, England, 1994).
- [27] L. Cavaleri, J. Alves, F. Ardhuin, A. Babanin, M. Banner, K. Belibassakis, M. Benoit, M. Donelan, J. Groeneweg, T. Herbers *et al.*, *Progr. Oceanogr.* **75**, 603 (2007).
- [28] E. Terray, M. Donelan, Y. Agrawal, W. Drennan, K. Kahma, A. Williams, P. Hwang, and S. Kitaigorodskii, *J. Phys. Oceanogr.* **26**, 792 (1996).
- [29] See the Supplemental Material at <http://link.aps.org/supplemental/10.1103/PhysRevLett.110.184504> for the animation of the simulation.